

Magnetically active transition metal cation-substituted alumina

Changning Li¹, Nicholas Ku², Yaohua Liu³, Jinbo Pan⁴, Binbo Chai¹, Feng Hu¹, Michael Kornecki², Qimin Yan^{4*}, Raymond Brennan^{2*}, and Shenqiang Ren^{1*}

¹ Department of Mechanical and Aerospace Engineering, Department of Chemistry, Research and Education in Energy Environment and Water (RENEW) Institute, University at Buffalo, The State University of New York, Buffalo, NY 14260, USA

² US Army Research Laboratory, Aberdeen Proving Ground, MD 21005, USA.

³ Quantum Condensed Matter Division, Oak Ridge National Laboratory, Oak Ridge, TN 37831, USA.

⁴ Department of Physics, Temple University, Philadelphia, PA 19122, USA

E-mail: shenren@buffalo.edu, raymond.e.brennan.civ@mail.mil, qiminyan@temple.edu.

Received xxxxxx

Accepted for publication xxxxxx

Published xxxxxx

Abstract

Alumina (Al_2O_3) is one of the most widely used ceramic materials for innumerable applications, due to its unique combination of attractive physical and mechanical properties. These intrinsic properties are dictated by the numerous phases that Al_2O_3 forms and its related phase transformations. Transition metal (TM) cation dopants [iron (Fe), cobalt (Co), nickel (Ni) and manganese (Mn)], even in sparse amounts, have been shown to significantly affect the phase transformation and microstructural evolution of Al_2O_3 . Small concentrations of TM cation dopants have successfully been incorporated to synthesize magnetically active Al_2O_3 , while reducing the θ to α phase transformation temperature by 150 °C, and maintaining the outstanding mechanical properties. In addition, first-principle calculations based on density-functional theory (DFT) with hybrid functional (HSE06) and the PBE+U methods have provided a mechanistic understanding of the formation energy and magnetism of the TM-doped α and θ phases of Al_2O_3 . The results reveal a potential route for phase transition regulation and external magnetic field-induced texturing of Al_2O_3 ceramics.

Keywords: Alumina, transition metal doping, magnetically active, phase transition

1. Introduction

In recent years, cation-doped Al_2O_3 has been extensively studied as an important ionic ceramic material for catalyst support[1-3], thermal-barrier coatings[4, 5], transparent armor[6, 7], and laser host materials[8], due to its excellent chemical, mechanical, and optical properties, all of which have been influenced by crystalline phases and microstructural characteristics (e.g., grain size). Dopant cations typically do not influence deformation of the crystal cell structure, but are known to impact the sintering thermodynamic behavior and grain growth of the desired

Al_2O_3 phase by entering the interspace (octahedral or tetrahedral sites) and/or replacing cations of the intrinsic crystal lattice, affecting the ionic bond energy[9, 10] and grain size[11]. It has been reported that mechanical properties, such as the abrasive resistance[12], can be increased with Al_2O_3 grain size reduction[13]. For dopant elements with net unpaired electrons, dopant ions can strengthen the coupling between micro-domains under external magnetic fields[14], improving the overall strength[15]. A distinct relationship between lanthanide (Ln) doping and microstructural evolution in Ln-doped Al_2O_3 has been experimentally described in our previous studies[16]. In this effort, the focus is on exploration

of Al_2O_3 doped with 3d transition metal (TM) cations, such as Fe, Co, Ni, and Mn, which have high magnetic moments, and similar radii to Al. In addition, magnetic TM dopants could potentially induce crystallographic texturing in Al_2O_3 materials. The microstructures and physical properties of TM-doped Al_2O_3 under different calcination temperatures have been studied with a combination of high-resolution X-ray Diffraction (HRXRD), X-ray Absorption Near-Edge Structure (XANES), electron microscopy, Vibrating Sample Magnetometry (VSM), and nano-indentation. To corroborate experimental findings, hybrid-functional based DFT calculations were also performed to aid in mechanistic understanding of phase transformations in TM-doped alumina.

2. Experimental Section

2.1 Sample Preparation

A wet chemical synthesis process via precipitation was utilized in a similar manner to Sanamyan et al [17]. The constituent elements investigated in this study were Fe, Co, Mn, and Ni. The metal salts used as cation sources for the synthesis were all commercially available products from Alfa Aesar (Haverhill, MA): aluminum nitrate nonahydrate [$\text{Al}(\text{NO}_3)_3 \cdot 9\text{H}_2\text{O}$] (99.999%), manganese (II) nitrate hydrate [$\text{Mn}(\text{NO}_3)_2 \cdot x\text{H}_2\text{O}$] (99.999%), iron (III) nitrate nonahydrate [$\text{Fe}(\text{NO}_3)_3 \cdot 9\text{H}_2\text{O}$] (99.999%), cobalt (II) nitrate hexahydrate [$\text{Co}(\text{NO}_3)_2 \cdot 6\text{H}_2\text{O}$] (99.999%), and nickel (II) nitrate hexahydrate [$\text{Ni}(\text{NO}_3)_2 \cdot 6\text{H}_2\text{O}$] (99.9985%). A solution was prepared in deionized H_2O with a nitrate concentration of 2.15 M. All of the TM-doped Al_2O_3 samples referenced in this study were prepared to form a composition with doping level around 400 ppm.

As shown in Figure 1a, acidic solutions of aluminum nitrate and TM nitrate, along with basic solutions of ammonium hydroxide ($\text{NH}_3 \cdot \text{H}_2\text{O}$) and ammonium bicarbonate (NH_4HCO_3) in deionized H_2O , were simultaneously added dropwise into a buffer solution with pH of 7. As the four solutions were combined in the buffer, particles of doped Al_2O_3 precursor began to precipitate out into suspension. The flow rate of the basic solution was adjusted to maintain the pH of the bath at 7 for the duration of the synthesis process. During the entire titration process, the suspension was mixed using a magnetic stir bar.

After the precipitation process was completed, the suspension was stirred overnight to allow the particles to ripen before being filtered through nitrocellulose paper. The collected particles were then dispersed in deionized H_2O and filtered two times to wash off any remnant salts from synthesis. Finally, the particles were dispersed in isopropanol and filtered to aid in the drying process, before being placed in an oven at 70°C . Once dried, the precursor powder was ground with a mortar and pestle.

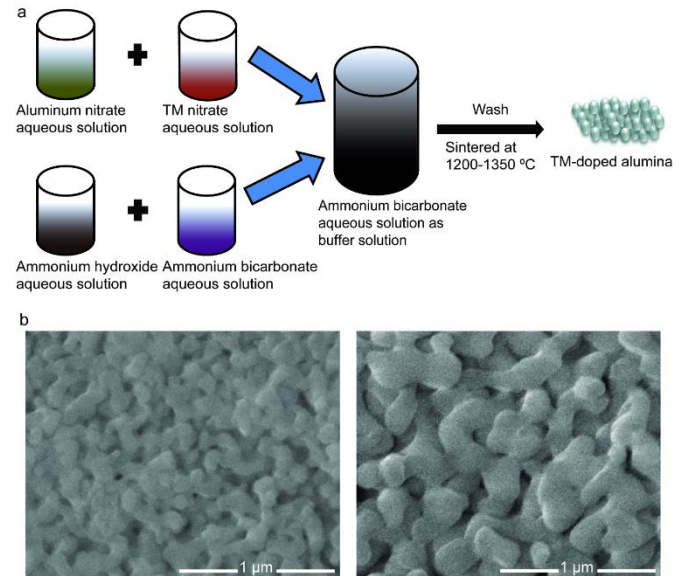


Figure 1. (a) Schematic representation of the TM-doped Al_2O_3 samples preparation process. (b) SEM images of Ni-doped Al_2O_3 under 1200°C (left) and 1350°C (right) respectively.

2.2 Material Characterization

HRXRD (Synchrotron 11-BM at the Advanced Photon Source of Argonne National Laboratory) was employed to examine the effect of doping on Al_2O_3 crystalline phase composition based on the TM species and sintering temperature. The TM species doped in the alumina samples *K*-edge XANES spectra were collected using linear polarized X-rays at the undulator beamline 20-ID-C of the Advanced Photon Source (APS) in Argonne National Laboratory. XANES spectra for TM standards used in linear combination fitting (LCF) of all XANES spectra were performed under the same beamlines. The phase evolution and grain size of TM-doped Al_2O_3 samples were further confirmed through a direct observation of the powder under an FRI Quanta450FEG SEM and TEM. The magnetization of the samples was characterized by a MircoSense EV7 high sensitivity vibrating sample magnetometer. Compressive force displacement curves and ultrafast extreme property mapping (XPM) images were measured with Hysitron TI 950 TriboIndenter/Nanoindenter and TI980 TriboIndenter with a diamond Berkovich tip. Optical transmittance of the samples was analysed using an Agilent Model HP8453 UV-vis spectrophotometer.

3. Results and Discussion

Of the many distinct crystalline phases of Al_2O_3 , the α -phase, which possesses a hexagonal closed packed (HCP) oxygen sub-lattice, has demonstrated remarkable hardness and been identified as the most thermodynamically stable.

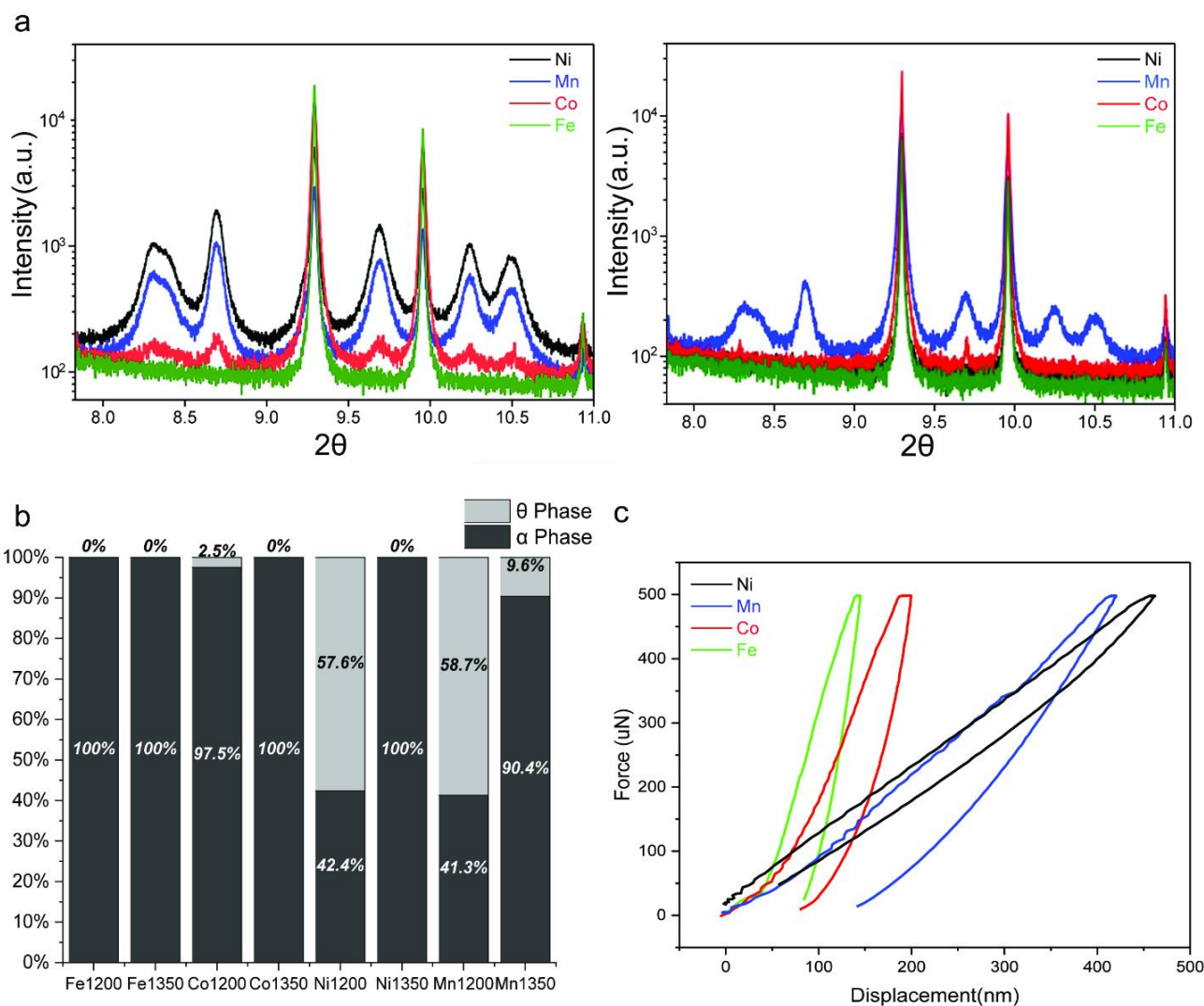


Figure 2. (a) HRXRD spectra of the TM-doped Al₂O₃ samples calcined under 1200°C (left) and 1350°C (right). (b) Rietveld refinement results on the percentages of α-phase and θ-phase. (c) Compressive stress-strain curves as the rigidity measurement results on TM cation-doped Al₂O₃ samples calcined under 1200°C.

All other metastable phases of Al₂O₃ irreversibly transform to α-phase under high temperature conditions (typically above 1300°C). The phase transition of Al₂O₃ can follow many paths, depending on the initiating alumina precursor, typically starting with a boehmite structure, and followed by the transition sequence of gamma (γ), delta (δ), theta (θ), and alpha (α) with increasing temperature [18]. TM-doped Al₂O₃ powders were synthesized following the procedures shown in Fig. 1a [12, 16]. Ammonium aluminum hydroxide carbonate (NH₄Al_{1-x}TM_x(OH)₂CO₃) was generated via an *in situ* precipitation method in an aqueous environment, and the resulting powder was dried and calcined at a set temperature in air. By precisely controlling the atomic ratios of TM-dopants, the concentrations of TM species were maintained at a constant level of TM_{0.0007}Al_{1.9993}O₃ (ca. 400 ppm), to avoid potential formation of TM aluminate and/or oxide phases. A

bi-modal size distribution was observed in all TM-doped Al₂O₃ samples (as shown in Fig. 1b, taking Ni-doped Al₂O₃ as an example, and Fig. S1), which indicated the presence of a mixture of crystalline phases in the powder samples. It was observed that the resulting crystalline phase composition did not solely rely on the dopant species, but was influenced by the calcination temperatures as well. HRXRD measurements were performed to confirm the crystalline phase compositions. In order to compare the effect of the dopant species on crystalline phase transformations (θ to α-phase transition), doped Al₂O₃ was calcined under different temperatures below 1350°C (the characteristic phase-transition temperature of pure Al₂O₃). It should be noted that when the calcination temperature was increased to 1350°C, Al₂O₃ with various dopants (with the exception of the Mn-doped samples) could be converted to α-phase.

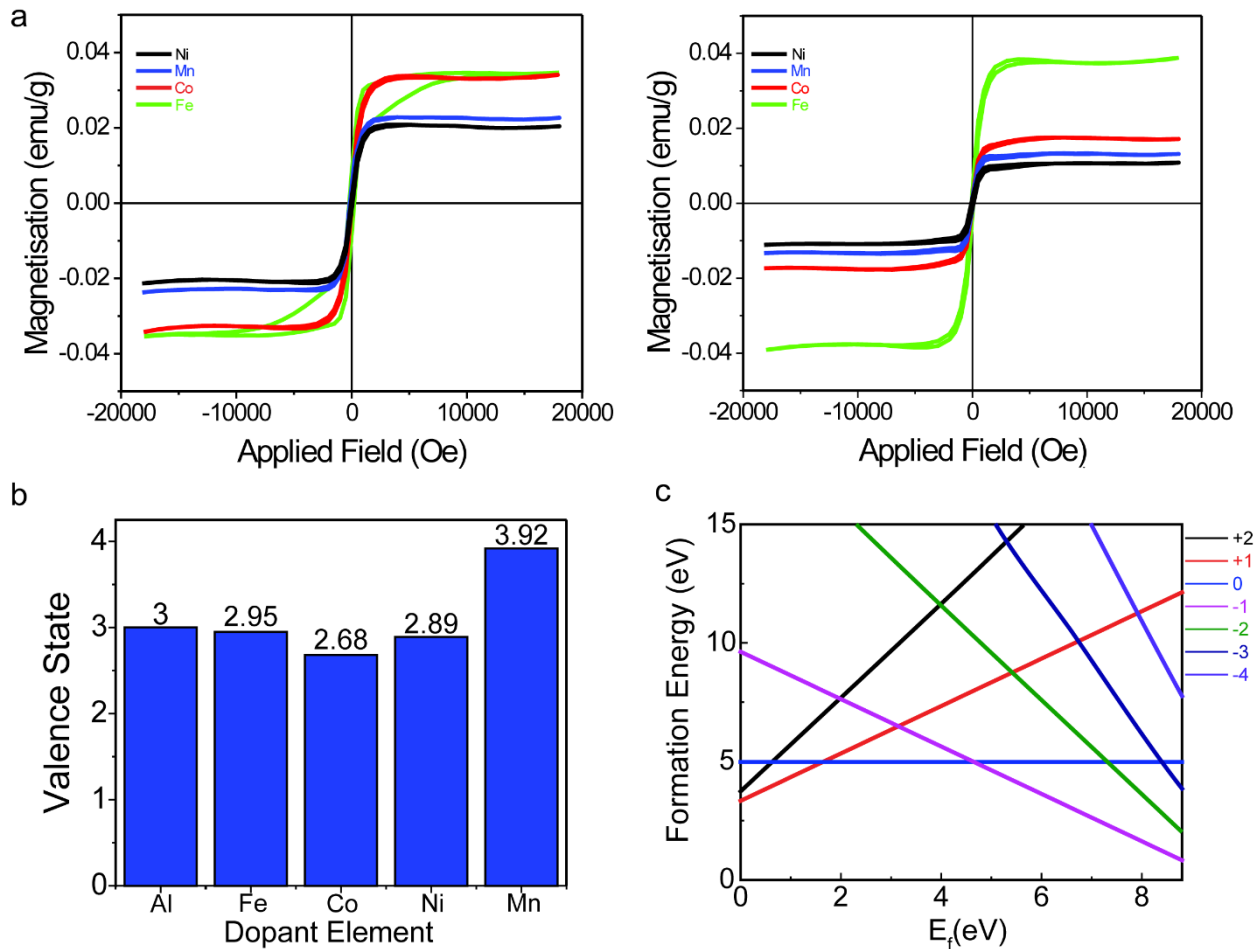


Figure 3. (a) MH loops of TM cation-doped alumina samples calcined under 1200°C (left) and 1350°C (right). (b) Valence states of TM cation dopant in the Al_2O_3 based on XANES spectra calculated from LCF with corresponding standard samples. (c) Formation energies as a function of Fermi level (E_f) for Fe-doped Al_2O_3 samples.

As evidenced in the corresponding HRXRD spectra (Fig. 2a), there were no notable θ -phase diffraction signals in the Fe-, Co-, and Ni-doped Al_2O_3 . These spectra were consistent with the size distribution of doped Al_2O_3 , where the α -phase dominated grains were represented by the uniform spherical shapes and dimensions. When the calcination temperature was decreased to 1200°C, the Fe- and Co-doped Al_2O_3 demonstrated homogeneous and uniform shapes, in accordance with the XRD spectra. The Co-doped Al_2O_3 prepared at 1200 °C suggested a notably larger portion of α -crystalline phase, while no θ -phase was observed in the Fe-doped Al_2O_3 . All θ -phase transitioned into α -phase for the Fe-doped Al_2O_3 , indicating a reduction in phase transition temperature by 150 °C, compared to that of pure Al_2O_3 . In addition, the X-ray Diffraction patterns confirmed that the crystalline structure of Al_2O_3 was not affected by doping. Based on these observations, all of the spectra were comparatively studied and analysed quantitatively by Rietveld refinement (Fig. 2b). Rietveld refinement was also utilized to obtain the crystallite phase composition for TM-doped Al_2O_3 .

At the calcination temperature of 1350°C, all θ -phase was transformed to α -phase in the Co- and Ni-doped samples, while 9.6% of θ -phase remained in the Mn-doped Al_2O_3 sample. In addition, the average grain sizes in the Co-, Ni- and Mn-doped Al_2O_3 samples were enlarged as a result of the θ -to- α -phase transition. All of the particles were approximately the same size before sintering (Fig. S2). Another noteworthy feature was that there were no detectable signals from TM aluminate and/or oxide phases, based on X-ray Diffraction spectra and energy dispersive X-ray (EDX) imaging and analysis (Fig. S3-S10). **Furthermore, the ratio of α -phase was consistent with the mechanical properties, as indicated by nano-indentation testing**, in which an external load was applied through a nano-indenter tip on the sample surface under force-control mode, resulting in a maximum force of 500 μN applied to the sample (Fig. 2c). The displacement distances of the Al_2O_3 samples increased with the ratio of θ -phase. The nano-indentation test, along with XPM (Fig. S11), and optical characterization (Fig. S12) suggested that the

structural properties of Al₂O₃ were not influenced by the introduction of TM cations.

The magnetic hysteresis loops of TM-doped Al₂O₃ demonstrated paramagnetic properties (Fig. 3a). The saturation magnetization (M_s) of TM-doped Al₂O₃ was matched with the extra-nuclear electron configuration of doping elements collected from XANES for Fe, Co, Mn and Ni. Based on the valence state characterization of TM-doped Al₂O₃ calcined at 1350 °C (Fig. 3b), according to the Pauli exclusion principle and Hund's Rules, the Fe cation indicated 4.950 unpaired electrons, while Co, Mn and Ni, indicated 3.676, 3.083 and 2.892 unpaired electrons, respectively. The same relative magnitude order was observed in TM-doped Al₂O₃ calcined at 1200°C. It should be noted that the Co, Mn, and Ni valence states in the calcined samples were higher than those of the chemicals selected as precursors. Oxidization occurred during the preparation process except for the Fe-doped samples, as Co²⁺, Ni²⁺ and Mn²⁺ were oxidized to +2.676, +2.892, and +3.917, respectively. The spin density distributions and net magnetic moments did not solely depend on the unpaired electrons of the dopant elements, but were also affected by the coupling interaction intensities of atomic magnetic moment in the solid TM-doped Al₂O₃ material. As such, regarding the trace dopant concentration in Al₂O₃, it may imply that the coupling interaction intensities of atomic magnetic moments in the TM cations were similar to that of hydrated cations in an aqueous solution. Taking into consideration that pure Al₂O₃ is diamagnetic, the paramagnetic signals from low TM concentrations in doped Al₂O₃, especially for Fe-doped at 1200°C, indicating the possibility of magnetic field texturing. In order to gain insight into the notable reduction of phase transition temperatures in Fe-doped Al₂O₃ samples, the formation energies of the θ - and α -phases were calculated as a function of the Fermi levels (E_f) using first-principles computations (Fig. 3c). The formation energy of the Fe impurity in Al₂O₃ at a charge defect q was calculated using DFT with the hybrid functional:

$$E_f = E_{\text{tot}} - E(\text{Al}_2\text{O}_3) + \mu_{\text{Al}} - \mu_{\text{Fe}} + q(E_F + \epsilon_v) + \Delta q$$

where E_{tot} is the total energy of the supercell containing Fe-doped Al₂O₃, $E(\text{Al}_2\text{O}_3)$ is the total energy of a perfect crystal in the same supercell, q is the charge state of the point defect, μ_{Al} and μ_{Fe} are chemical potentials of Al and Fe atoms (-4.37 and -13.05 eV, obtained from the total energies of elemental Al and Fe, respectively), E_F is the Fermi level, and ϵ_v is the energy of valence band maximum. Note that the choice of chemical potentials does not affect the positions of thermodynamic charge-state transition levels. It was clear that substitutional Fe impurities could exist in Al₂O₃ samples at -, 0, and + charge states, depending on the Fermi level of the samples. The magnetic moment on the Fe atom was calculated as 1 Bohr magneton for neutral impurity and 2 Bohr magnetons for dopants in the - charge state. For the case of

Table 1. The calculated energy difference between θ and α phases of pure Al₂O₃ and Fe-doped Al₂O₃ systems in supercells containing 48 aluminum and 72 oxygen atoms.

DFT Methods	Energy difference ($dE = (E_{\text{tot}}(\theta) - E_{\text{tot}}(\alpha))$ (eV))	
	Pure Al ₂ O ₃	Fe-doped Al ₂ O ₃
HSE06	3.000	4.881
PBE+U	1.048	1.522

neutral impurities, the relative energy difference between the two phases was calculated, and it was observed that Fe-doping could further increase the energy difference and effectively stabilize the α -phase (Table 1). This conclusion was confirmed by two computational methods, including the HSE06 and PBE+U methods, as shown in Table 1. The temperature effects on the total energy change due to entropy were not included in the calculations, as they were known to reduce the energy differences between the two phases, but this would not influence the conclusion on relative phase stability either way.

4. Conclusion

It was demonstrated that sintering of Al₂O₃ could be significantly influenced by the presence of transition elements, providing insight into how phase transformations and microstructural evolution varied with dopant species (based on systematic studies of Fe, Ni, Co, and Mn cation-doped Al₂O₃ materials). This was observed during the heat treatment process, and verified by first-principles computations. A relationship between the unpaired electrons of the doped TM cations and the macroscopic properties was reported experimentally. By adding a sparse amount of 3d TM dopants, diamagnetic Al₂O₃ became magnetically active, showing the potential of controlling the texture of bulk Al₂O₃ ceramics in the presence of external magnetic fields without sacrificing mechanical and optical properties.

Acknowledgements

Financial support was provided by the U.S. Army Research Office supports S. R. under Award W911NF-18-2-0202. Use of the Advanced Photon Source (11-BM) at Argonne National Laboratory was supported by the U. S. Department of Energy, Office of Science, Office of Basic Energy Sciences, under Contract No. DE-AC02-06CH11357. Work at ORNL was supported by the Division of Scientific User Facilities of the Office of Basic Energy Sciences (BES), US Department of

Energy (DOE). The research reported in this document was performed in connection with contract/instrument W911QX-16-D-0014 with the U.S. Army Research Laboratory. The views and conclusions contained in this document are those of Service Engineering and the U.S. Army Research Laboratory. Citation of manufacturer's or trade names does not constitute an official endorsement or approval of the use thereof. The U.S. Government is authorized to reproduce and distribute reprints for Government purposes notwithstanding any copyright notation hereon.

References

1. Peterson, E.J., et al., *Low-temperature carbon monoxide oxidation catalysed by regenerable atomically dispersed palladium on alumina*. Nature communications, 2014. **5**: p. 4885.
2. Garbarino, G., et al., *Ethanol and diethyl ether catalytic conversion over commercial alumina and lanthanum-doped alumina: Reaction paths, catalyst structure and coking*. Applied Catalysis B: Environmental, 2018. **236**: p. 490-500.
3. Toyao, T., et al., *Catalytic NO-CO Reactions over La-Al₂O₃ Supported Pd: Promotion Effect of La*. Chemistry Letters, 2018. **47**(8): p. 1036-1039.
4. Matsudaira, T., et al., *Oxygen permeability in cation-doped polycrystalline alumina under oxygen potential gradients at high temperatures*. Acta Materialia, 2011. **59**(14): p. 5440-5450.
5. Evans, A.G., et al., *Mechanisms controlling the durability of thermal barrier coatings*. Progress in materials science, 2001. **46**(5): p. 505-553.
6. Grujicic, M., W. Bell, and B. Pandurangan, *Design and material selection guidelines and strategies for transparent armor systems*. Materials & Design, 2012. **34**: p. 808-819.
7. Salem, J.A., *Transparent armor ceramics as spacecraft windows*. Journal of the American Ceramic Society, 2013. **96**(1): p. 281-289.
8. Penilla, E.H., et al., *Gain in polycrystalline Nd-doped alumina: leveraging length scales to create a new class of high-energy, short pulse, tunable laser materials*. Light: Science & Applications, 2018. **7**(1): p. 33.
9. Andersson, J.M., et al., *Ab initio calculations on the effects of additives on alumina phase stability*. Physical Review B, 2005. **71**(1): p. 014101.
10. Mortazavi, N., et al., *Interplay of water and reactive elements in oxidation of alumina-forming alloys*. Nature materials, 2018: p. 1.
11. Pint, B., J.a. Martin, and L. Hobbs, *18 O/SIMS characterization of the growth mechanism of doped and undoped α -Al₂O₃*. Oxidation of metals, 1993. **39**(3-4): p. 167-195.
12. Rainforth, W., *The wear behaviour of oxide ceramics-A Review*. Journal of materials science, 2004. **39**(22): p. 6705-6721.
13. Krell, A., et al., *Transparent sintered corundum with high hardness and strength*. Journal of the American Ceramic Society, 2003. **86**(1): p. 12-18.
14. Nykwest, E.C., et al., *Magnetic and energetic properties of transition metal doped alumina*. Journal of Physics: Condensed Matter, 2018. **30**(39): p. 395801.
15. Li, Q., et al., *Rise and fall of ferromagnetism in O-irradiated Al₂O₃ single crystals*. Journal of Applied Physics, 2015. **117**(23): p. 233904.
16. Patel, K., et al., *Structural effects of lanthanide dopants on alumina*. Scientific reports, 2017. **7**: p. 39946.
17. Sanamyan, T., et al., *Spectroscopic properties of Er³⁺-doped α -Al₂O₃*. Optical Materials, 2013. **35**(5): p. 821-826.
18. Wefers, K. and C. Misra, *Oxides and Hydroxides of Aluminum.(Report)*. Aluminum Company of America, 92, 1987: p. 1987.